ACS APPLIED MATERIALS & INTERFACES
Research Article
www.acsami.org

Correlation between Surface Chemistry, Density, and Band Gap in Nanocrystalline WO_3 Thin Films

R.S. Vemuri,[†,‡,§] M.H. Engelhard,[§] and C.V. Ramana*[,†,‡]

[†]Department of Mechanical Engineering and [‡]Department of Materials Science and Engineering, University of Texas at El Paso, El Paso, Texas 79968, United States

[§]Environmental Molecular Sciences Laboratory (EMSL), Pacific Northwest National Laboratory (PNNL), Richland, Washington 99352, United States

ABSTRACT: Nanocrystalline WO_3 thin films were produced by sputter-deposition by varying the ratio of argon to oxygen in the reactive gas mixture during deposition. The surface chemistry, physical characteristics, and optical properties of nanocrystalline WO_3 films were evaluated using X-ray photo-electron spectroscopy (XPS), scanning electron microscopy (SEM), atomic force microscopy (AFM), X-ray reflectivity (XRR), and spectrophotometric measurements. The effect of ultramicrostructure was significant on the optical properties of WO_3 films. The XPS analyses indicate the formation of stoichiometric WO_3 with tungsten existing in fully oxidized valence state (W^{6+}). However, WO_3 films grown at high oxygen concentration (>60%) in the sputtering gas mixture were over stoichiometric with excess oxygen. XRR simulations based on isotropic WO_3 film−SiO_2 interface−Si substrate modeling indicate that the density of WO_3 films is sensitive to the oxygen content in the sputtering gas. The spectral transmission of the films increased with increasing oxygen. The band gap of these films increases from 2.78 to 3.25 eV with increasing oxygen. A direct correlation between the film density and band gap in nanocrystalline WO_3 films is established on the basis of the observed results.

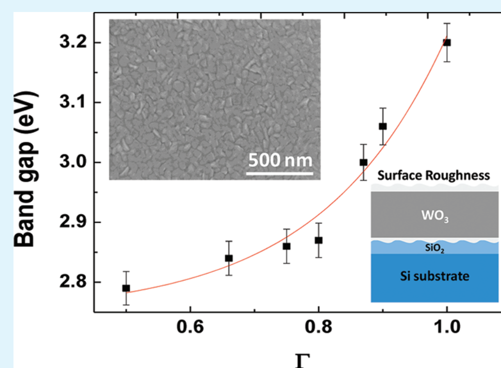

KEYWORDS: *WO_3 thin films, surface chemistry, XPS density, X-ray reflectivity, spectrophotometry, optical properties, band gap*

1. INTRODUCTION

Tungsten oxide (WO_3) is an intensely studied representative of a group of "chromogenic" materials because of the coloration effects associated with various processes.[1−6] There has been a great deal of recent interest in low-dimensional structures of WO_3 for a wide variety of applications in optoelectronics, microelectronics, selective catalysis, and environmental engineering.[2−20] WO_3 has been in use for the development of smart windows for energy-efficient architecture of buildings and automobiles, flat-panel displays, optical memory and writing−reading−erasing devices, and electronic information displays.[1−6] It has been demonstrated that WO_3 films exhibit chemical sensing properties that have numerous applications in environmental and industrial pollution monitoring.[7−18] WO_3 films exhibit excellent functional activity to various gases (e.g., H_2S, NO_x, trimethylamine, and other organics) and are suitable for use in integrated sensors.[13−18] Most recently, the attractive properties of WO_3-based materials have increased their consideration for application in photoelectrochemical cells (PECs) for hydrogen production by water splitting.[19−21] In addition, Zheng et al. have proposed and demonstrated new applications of WO_3 in emerging dye-sensitized solar cells (DSSC) technology.[22] Although the efficiency is not comparable to those that employ the best known TiO_2-based DSSCs, there are options to tailor the microstructure and chemistry in order to improve the efficiency.[22] A very detailed account of structure, synthesis, and application of nanostructured WO_x can be found in a current review article where the opportunities and scope for further exploitation of nanostructured WO_3 materials in emerging technological applications is presented.[23]

WO_3 is a complicated material with respect to crystal structure and thermal stability because of several structures, such as monoclinic, triclinic, tetragonal, orthorhombic, cubic, and hexagonal for pure and oxygen deficient WO_3.[1−3,24−28] At room temperature, WO_3 crystallizes in a triclinic structure and exhibits structural transformation at higher temperatures. Investigations on bulk WO_3 report the following sequence: triclinic (∼30 °C) → monoclinic (330 °C) → orthorhombic (740 °C) → tetragonal.[1,3,24−29] Additionally, formation of pyrochlore WO_3 structure at about 373 K has been reported.[30] The ideal WO_3 crystal structure can be represented as a cubic ReO_3 structure.[31,32] In fact, the polymorphs of WO_3 can be described as distortions from the cubic ReO_3 structure.[1,24−29] However, WO_3 thin films prepared by a wide variety of chemical and physical techniques employing various processing conditions usually exhibit different crystal structure, morphology, surface/interface chemistry, and electronic and electrochemical properties.[1−17,33−40]

Received: November 22, 2011
Accepted: January 10, 2012
Published: February 14, 2012

© 2012 American Chemical Society

The optical, photochemical, and electrical properties of metal oxide thin films grown from chemical or physical vapor deposition methods are sensitive to the physical and chemical characteristics, which in turn depend on the processing conditions and precursor materials. For instance, the density and index of refraction for TiO_2, SiO_2 HfO_2, and ZrO_2 thin films was shown to be sensitive to the processing conditions.[41−43] From this point of view, a detailed understanding and control over the physical parameters (e.g., crystal structure and density) and chemical parameters (e.g., valence state of W ions and composition) in WO_3 thin films is required in order to optimize performance for a given application. The present work was, therefore, performed on sputter-deposited nanocrystalline WO_3 films under varying the oxygen partial pressure at a fixed deposition temperature. Earlier we reported on the effect of deposition temperature on the microstructure and electrical properties of nanocrystalline WO_3 films.[34−36] We found that the effect of growth temperature is significant on the structure, phase, grain-size and electrical conductivity of nanocrystalline WO_3 films.[34−36] The objective of the present work is to derive a detailed understanding of the surface chemistry, density and optical properties, which will have profound influence on the optical, electronic, and photochemical device performance of WO_3 films. Interestingly, a correlation is found between surface chemistry, density, and band gap in nanocrystalline WO_3 films as presented and discussed in this paper.

2. EXPERIMENTAL SECTION

A. Fabrication. WO_3 thin films were deposited onto optical grade quartz and silicon (Si) (100) wafers by radio frequency (RF) (13.56 MHz) magnetron sputtering. All the substrates were thoroughly cleaned using the standard procedure reported elsewhere,[34] and dried with nitrogen before introducing them into the vacuum chamber. The chamber was initially evacuated to a base pressure of $\sim 1 \times 10^{-6}$ Torr. Tungsten (W) metal target (Plasmaterials Inc.) of 3" diameter and 99.95% purity was employed for reactive sputtering. The W-target was placed on a 3 in. sputter gun, which is placed at a distance of 8 cm from the substrate. A sputtering power of 40 W was initially applied to the target while introducing high-purity argon (Ar) into the chamber to ignite the plasma. Once the plasma was ignited, the power was increased to 100 W and oxygen (O_2) was released into the chamber for reactive deposition. The flow of the Ar and O_2 and their ratio was controlled using as MKS mass flow meters. Before each deposition, the W-target was presputtered for 10 min using Ar alone with shutter above the gun closed. The samples were deposited by varying the oxygen content in the reactive gas mixture while keeping the deposition temperatures (T_s) fixed at 400 °C. Specifically, the oxygen gas fractionation ratio [$\Gamma = O_2/Ar+O_2$] is varied in order to study the effect of oxygen gas flow rate on the structure and optical properties of WO_3 films. The deposition was made for a constant time of 60 min. The substrates were heated by halogen lamps and the desired temperature was controlled by an Athena X25 controller.

B. Characterization. The grown WO_3 films were characterized by performing structural and optical measurements. Surface imaging analysis was performed using a high-performance and ultra high resolution scanning electron microscope (Hitachi S-4800). Secondary electron imaging was performed on WO_3 films grown on Si wafers using carbon paste at the ends to avoid charging problems. The grain detection, size-analysis and statistical analysis was performed using the software provided with the SEM. X-ray reflectivity (XRR) measurements were performed using a Bruker Discover D8 X-ray diffractometer. Samples grown on Si substrates were employed for XRR measurements. All the measurements were made ex situ as a function of partial pressure. The thickness and density calculations were performed by fitting the XRR data using LEPTOS software. The film thickness was obtained by the period of oscillations in the XRR curve. The film-density was determined by the position of total reflection edge. Surface imaging was also performed using an atomic force microscope (AFM) (Nanoscope IV-Dimension 3100 SPM system). WO_3 films grown on Si wafers were used for AFM analysis. The main purpose of AFM measurements was to obtain quantitative information on the surface roughness and compare with the results of XRR fitting.

XPS measurements were performed with a Physical Electronics Quantera scanning X-ray microprobe. This system uses a focused monochromatic Al Kα X-ray (1486.7 eV) source for excitation and a spherical section analyzer. The instrument has a 32 element multichannel detection system. A 100 W X-ray beam focused to 100 μm diameter was rastered over a 1.4 mm × 0.1 mm rectangle on the sample. The X-ray beam is incident normal to the sample and the photoelectron detector is at 45° off-normal. High energy resolution spectra were collected using a pass-energy of 69.0 eV with a step size of 0.125 eV. For the Ag 3d5/2 line, these conditions produced a fwhm of 0.91 eV. The sample experienced variable degrees of charging. Low energy electrons at ∼1 eV, 20 μA and low energy Ar^+ ions were used to minimize this charging.

The optical properties of WO_3 films were evaluated using optical transmission and reflectance measurements using Cary 5000 UV−vis-NIR double-beam spectrophotometer. Films grown on optical grade quartz were employed for optical property measurements. The quartz substrates employed extends the transparency range down to ∼190 nm and determining the absorption edge extending into ultraviolet (UV) region, which is more than sufficient to determine the band gap shift in deficient or stoichiometric or metal incorporated WO_3 films.

3. RESULTS

A. Surface Chemistry − XPS. X-ray photoelectron spectroscopy (XPS) data indicate that the WO_3 films are stoichiometric within a certain range of oxygen content in the reactive gas mixture while it becomes overstoichiometric for higher oxygen content. An XPS survey spectrum of a representative sample ($\Gamma = 0.9$) is shown in Figure 1. The XPS curve of as-grown sample (Figure 1a; lower panel) indicates that W and O were the main constituent elements of the samples, except for the C present in the sample surface. The C 1s peak observed at a binding energy (BE) of 284.6 eV for as-grown samples originates from surface adsorbed carbon species. It can be seen in the XPS curve (Figure 1b; upper panel) of the same sample that was sputtered for a few minutes with 2 kV Ar^+ ions that it shows no signal from C 1s level. This is a clear indication that the carbon presence is a result of adsorbed species on the film surface due to sample handling and can be removed with a light sputtering of the surface with low-energy Ar^+ ions.

The detailed core-level spectra of W 4f and O 1s peaks for WO_3 films are shown in Figure 2. For WO_3 films grown with $\Gamma = 0.5-0.9$, the XPS W 4f core-level peak exhibits a well-resolved doublet corresponding to W $4f_{5/2}$ and W $4f_{7/2}$ (Figure 2; upper panel) at the binding energy values of 37.9 and 35.8 eV, respectively. The W $4f_{7/2}$ peak at 35.8 eV in this work is in good agreement with the literature value of 35.7 eV characterizing the W^{6+} state in WO_3.[44−46] The corresponding O 1s core level peak at BE∼530.5 eV (Figure 2; lower panel) is the typical of O atoms bonded to W.[47,48] Absence of any other contributions, such as surface adsorbed oxygen or carbonyl groups, can be noted. Also, the O 1s core level is symmetric for all the samples reflecting the characteristic feature of O atoms bonded with W atoms only. The chemical composition determined using integrated peak areas and sensitive factors indicate that the O/W ratio was maintained well in the films grown at $\Gamma = 0.5-1.0$. However, it was noted that for samples under 2 kV Ar^+ sputtering i.e., after the removal of a few top surface layers, the oxygen to tungsten atomic ratio in WO_3 films is always higher

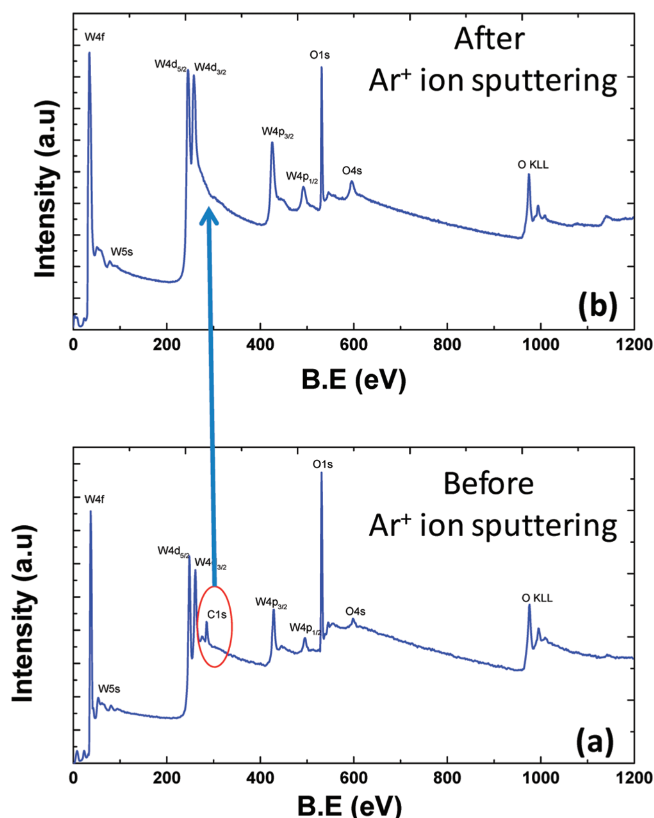

Figure 1. XPS survey spectra of WO_3 films. The survey spectrum obtained (a) before Ar^+ ion sputtering and that obtained (b) after sputtering are shown. The X-ray photoemission and Auger peaks and their respective binding energy positions are as indicated. It is evident that the C 1s peak disappears after Ar^+ ion sputtering indicating the adsorbed carbon on the samples surface.

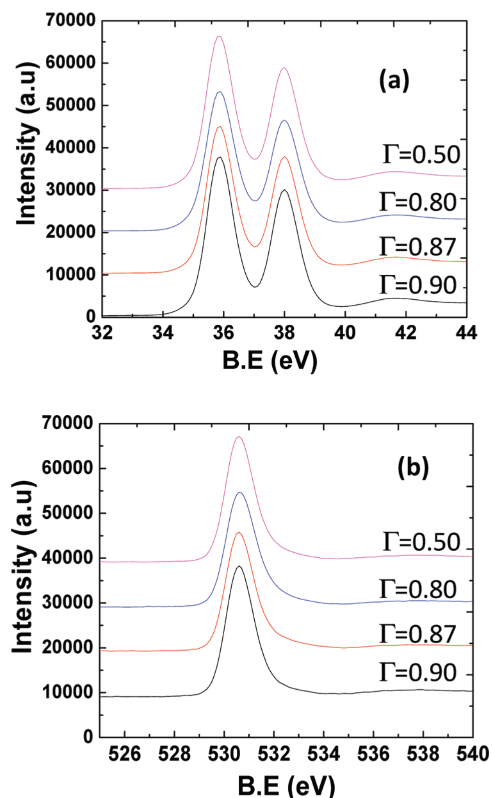

Figure 2. Core level XPS spectra of (a) W 4f and (b) O 1s.

than expected for those samples grown at $\Gamma \geq 0.6$. This observation indicates that there is excess oxygen trapped during the successive layer formation during film growth.

B. Film density and surface/interface structure – XRR, SEM, and AFM. The XRR patterns of WO_3 films are shown in Figure 3. Simulation of the XRR experimental data using appropriate models can provide physio-chemical information of the nanocrystalline WO_3 films. Specifically, the surface and interface roughness, thickness and density of the WO_3 films can be obtained from XRR spectra.[49] The density can be obtained from the total reflection or critical edge.[49] Film thickness can be derived from the period of the oscillations in the XRR spectra. In the present case, it is evident that the experimental and simulation curves are in excellent agreement for WO_3 films (Figure 3). The stack model used to simulate the spectra is shown in the inset of Figure 3a. The model contains, from top, WO_3 film, SiO_2 interface and Si substrate. The surface and interface roughness were also considered in order to accurately fit the experimental XRR spectra of WO_3 films. The following observations can be made from the XRR spectra (Figure 3). A positive shift (higher angle) of the critical edge with increasing oxygen flow rate is the first. The oscillations extend toward higher angle (>2°) is the second. The latter observation indicates that the film roughness is not very high. The positive shift of the critical edge indicates an increase in the film density with increasing oxygen content in the reactive gas mixture. The density varies in the range of 4.98–5.98 g/cm^3.

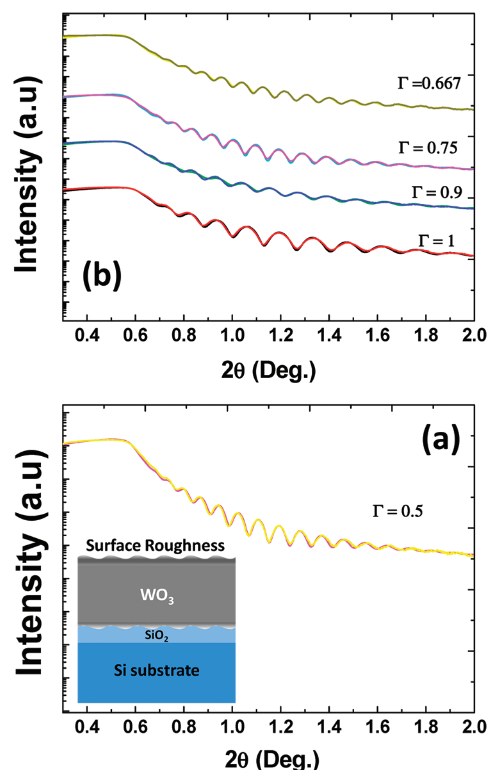

Figure 3. XRR experimental simulation curves of nanocrystalline WO_3 films. (a) The fitting procedure and the stack model employed are shown for films grown at $\Gamma = 0.5$. (b) The XRR curves and fitting is shown for a series of WO_3 films grown at variable oxygen concentration values.

dx.doi.org/10.1021/am2016409 | ACS Appl. Mater. Interfaces 2012, 4, 1371–1377

The film thickness and interfacial oxide thickness were also determined from XRR analysis. The variation of film thickness as a function of oxygen concentration is shown in Figure 4. It is

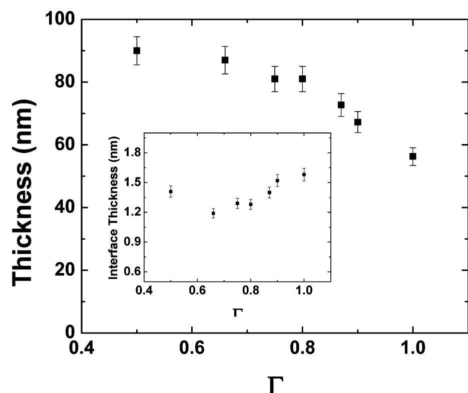

Figure 4. Variation WO_3 film thickness with oxygen concentration in the sputtering gas mixture. A continuous decrease in film thickness with increasing oxygen concentration can be noted. Inset shows the variation of interfacial SiO_2 thickness with Γ values.

evident that the film thickness decreases with increasing oxygen concentration. However, although the growth part is not very significant, a slightly increasing trend for interfacial oxide (SiO_2) with increasing oxygen concentration can be seen in the inset. Increasing oxygen pressure reduces the energy that the particles attain to the substrate and their mobility, making it more difficult for the sputtering species to bombard the substrate and, thus, leading to decreasing film thickness. During sputtering process, the target species are subjected to collisions with ambient gas molecules and other ejected atoms. The reactive sputter-gas, therefore, impedes the mobility and trajectory of sputtered species.

SEM images of nanocrystalline WO_3 films are shown in Figure 5. The fine microstructure and uniform distribution

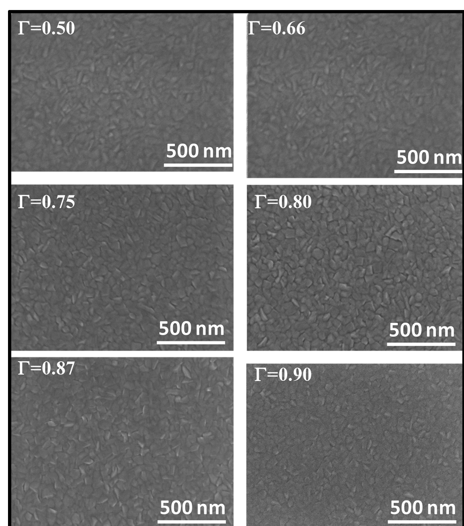

Figure 5. High-resolution SEM images of WO_3 films as a function of oxygen concentration in the sputtering gas mixture.

characteristics of the particles are evident in the micrographs (Figure 5). The X-ray diffraction (XRD) data (not shown) confirmed that these are crystalline grains. The average grain size, determined from XRD, gradually decreases with increasing oxygen flow rate. The grain size increases from 21 to 25 nm with increasing Γ to 0.65, at which point the grain size exhibits a decreasing trend to attain the lowest value of 15 nm at Γ = 1. The corresponding roughness and the randomness of the grains decrease with increasing oxygen content. Variation of the film surface roughness with oxygen concentration is presented in Figure 6. The values were determined from the XRR data

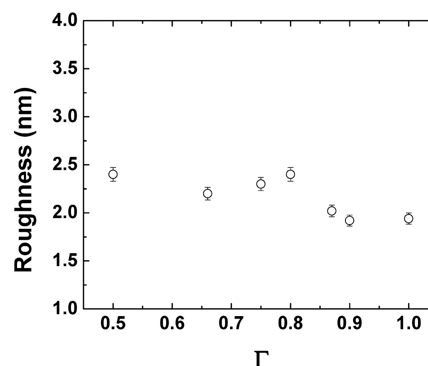

Figure 6. WO_3 film surface roughness determined from XRR.

where the surface roughness is varied order to obtain a best fit the experimental and simulation curves. The surface roughness values and their variation agrees well with the root-mean-square (rms) value surface roughness values obtained from AFM (not shown). It can be seen that the surface roughness decreases slightly with increasing oxygen concentration in the sputtering gas mixture.

C. Band Hap – Spectrophotometry. The optical transmittance spectra of WO_3 films are shown in Figure 7. The spectral

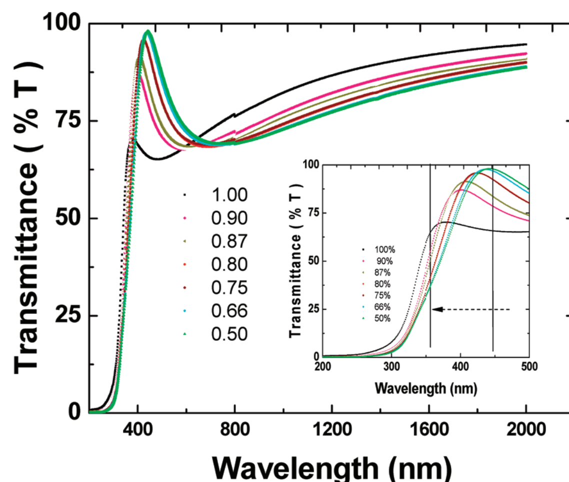

Figure 7. Spectral transmittance characteristics of WO_3 films as a function of oxygen concentration in the sputtering gas mixture. Inset shows the shift noted in the curves, as pointed by arrow, with increasing oxygen concentration.

transmission curves reveal the following characteristic features. (1) WO_3 films in general show a high transparency in the spectral region except where the incident radiation is absorbed across the band gap (E_g). This observation indicates the high-quality and transparent nature of WO_3 films. (2) An increase in optical transmittance with increasing oxygen content in the

reactive gas mixture. Inset in Figure 7 shows the expanded version of the transmittance spectra in a selected spectral region to show the effect of Γ values. The behavior indicates that the effect of oxygen concentration in the sputtering gas influences the optical properties. (3) The oxygen content also influences the absorption across the band gap. It is evident that the absorption edge shifts to lower spectral region indicating that the increasing oxygen increases the energy of the absorption edge. An arrow with a window is presented as shown in inset of Figure 7 to indicate the absorption edge shift as a function of increasing Γ values.

A further analysis of the optical spectra is performed in order to better understand effect of oxygen content in the reactive gas mixture on the optical properties and to derive a quantitative structure−property relationship. It is well-known that the optical absorption below E_g follows an exponential behavior.[1,5,34,49] The absorption, therefore, is exponentially dependent on the energy ($h\nu$) of incident photon in that region. For WO_3, in the E_g region (high absorption) or above the fundamental absorption edge, the absorption follows a power law of the form[1,5,34,50]

$$(\alpha h\nu) = B(h\nu - E_g)^2$$

{1}where $h\nu$ is the energy of the incident photon, α the absorption coefficient, B the absorption edge width parameter, E_g the band gap. The optical absorption coefficient, α, of the films is evaluated using the relation[34,49,50]

$$\alpha = [1/t]\ln[T/(1 - R)^2]$$

{2}where T is the transmittance, R the reflectance, and t the film thickness. The thickness values determined from XRR were employed to obtain the optical absorption coefficient of nanocrystalline WO_3 films. The absorption data and the plots obtained for WO_3 films are shown in Figure 8. It is evident that $(\alpha h\nu)^{1/2}$ vs $h\nu$ results in linear plots in the high absorption region, $\alpha > 1 \times 10^4$ cm^{-1}, suggesting indirect allowed transitions across E_g of WO_3 films. Regression analysis and extrapolating the linear region of the plot to $h\nu = 0$ provide the band gap value as indicated with an arrow in Figure 8. The E_g values derived from curves shown in Figure 8 increases from 2.78 to 3.25 eV with increasing Γ values.

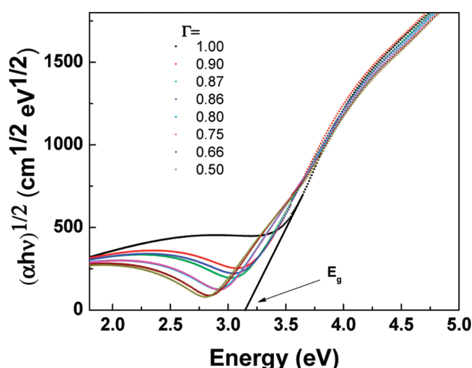

Figure 8. $(\alpha h\nu)^{1/2}$ vs $h\nu$ plots for WO_3 films grown at various oxygen concentration values. Extrapolating the linear region of the plot to $h\nu = 0$ provides the band gap value as indicated with an arrow.

4. DISCUSSION

The chemistry−density−band gap (optical property) relationship in nanocrystalline WO_3 films can be derived on the basis of the observed results and taking the simultaneous effect of oxygen content in the sputtering gas mixture and, hence, the associated effects into account. A decrease in film thickness with increasing oxygen concentration in the sputtering gas mixture indicates that the effective number of species ejected from target surface and the effective number of particles reaching and attaining the substrate decreases with increasing Γ values. It can be seen that increasing oxygen concentration reduces the energy that the particles attain to the substrate and their mobility. As such, it more difficult for the sputtering species to bombard the substrate and, thus, leads to a decreasing growth rate that in turn reduces film thickness.[41,42] It must be pointed out that during sputtering process, the target species are subjected to collisions with ambient gas molecules and other ejected atoms. This behavior results in a partial loss of energy and direction on their respective paths, which makes it more difficult to attain the substrate. The reactive sputter-gas, therefore, impedes the mobility and trajectory of sputtered species. Furthermore, at a given or constant sputter-power, increasing oxygen pressure in the plasma shifts the thermalization region toward the target.[41−43,51] As a result, oxidation of the W target takes place leading to a decrease in deposition rate and, hence, thickness of WO_3 films. A faster decrease in the growth rate of WO_3 films at higher oxygen concentration can then be attributed to the combined effect of target oxidation, sputter-ejected species being impeded, decrease in the mean free path, and partial resputtering of the film.

The results obtained from XRR and spectrophotometry indicates that the oxygen content in the reactive gas mixture influences the density and band gap. To explain the observed results and derive the correlation, we show the variation in the density and band gap of WO_3 films with Γ in Figure 9. The most important and very first observation is that these two parameters exhibit similar functional dependence on Γ value. Second, the density and band gap data was found to fit to an exponential growth function. The results can be explained as follows. It should be noted that the measured density of the WO_3 films is less compared to that bulk of the tungsten oxide (7.16 g/cm^3).[1,52] On the other hand the density increases with increasing oxygen concentration is sputtering gas mixture. The lower values of density may be due to voids in the grains. Also, the density of vapor deposited thin films is always lower than that of bulk counterparts. The increase in density with increasing Γ values can be attributed to the incorporation of excess oxygen that is trapped during the successive layer formation leading to the total film thickness. Evidence for this comes from the XPS analyses where the superstoichimetry for films grown at Γ > 0.6 is noted. We believe the excess oxygen trapped is also responsible for the observed behavior of E_g values for nanocrystalline WO_3 films. In WO_3, E_g corresponds to electronic transitions from the top of valence band (formed by the filled O 2p orbitals) to the conduction band (formed by the empty W 5d orbitals).[1,5,34,50,52,53] Reduction in the band gap can be expected in the presence of oxygen vacancies or any other structural defects. As such, the lower density coupled with the observed lower E_g values can be attributed to the present of voids or vacancies. The increase in density and band gap with a progressive increase in oxygen concentration can be attributed to the excess oxygen. It has been argued that the extra oxygen atoms in the defect picture can be viewed as interstitials.[52] In fact, we believe this is indeed the case in our WO_3 films. This is based on the fact that there is a higher O/W ratio in XPS. This extra oxygen is responsible to decrease the grain size and shifts the E_g values to higher energy side. This is the reason why WO_3

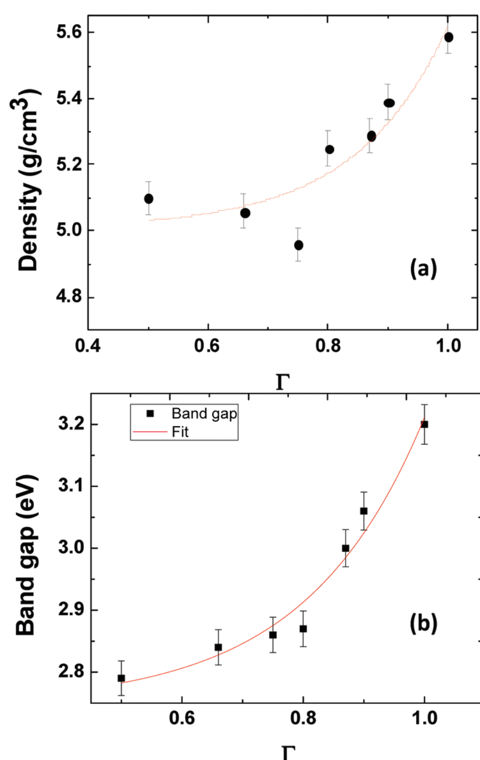

Figure 9. Comparison of (a) the trend of density variation and (b) band gap variation with oxygen concentration in sputtering gas mixture in nanocrystalline WO_3 films. A direct correlation between density and band gap in addition to similar trend can be noted. The density and band gap variation with oxygen concentration in the sputtering gas mixture follows an exponential growth function as indicted by lines.

films grown at higher oxygen concentration becomes more insulating, i.e., higher E_g, compared those grown at lower oxygen concentration. The presence of excess oxygen in sputtered grown oxides has been reported several times.[54−59] For instance, reactive sputtering of alumina films resulted in excess oxygen when sputtering was performed in the reactive oxygen atmosphere using Al target.[54] Using Rutherford backscattering spectrometry analysis, Chin et al have demonstrated the O/Ce ratio >2 in sputtered CeO_2 films.[55] Vink et al. have shown evidence for excess oxygen, which also helps lithium trapping, in sputtered WO_3 films.[56] Higher concentrations of oxygen chemisorbed on the film surface and along depth of the film leading to an increase in electrical conductivity has been reported for ZnO.[57] However, in the case of WO_3 films, the debate was on the presence of hydroxyl bonds[58,59] or the inherent processing effect of sputter-deposition[56] that accommodates the excess oxygen. XPS analysis of our WO_3 films did not reveal the presence of hydroxyl groups and the mechanism or the source of hydroxyl bonds for excess oxygen can, therefore, be ruled out. Our results are in close agreement with those reported by Venk et al.,[56] where it was claimed that the excess oxygen in the films is due to higher oxygen concentration and higher sputtering power, which are needed for incorporating the oxygen.[54−56] Specifically, the excess oxygen originates from negative ion effects, which is common in the oxygenated metal targets. As reported by Venk et al., negative oxygen ions are generated at the surface of the oxygenated targets.[56] These ions are accelerated and subsequently neutralized in the plasma. By virtue of their kinetic energy, the oxygen atoms can be incorporated in the growing film leading to the observed excess oxygen. A significant decrease in growth rate and film thickness (Figure 4) at higher oxygen concentration is direct evidence for the above-mentioned mechanism and excess oxygen incorporation into the growing WO_3 films.

5. CONCLUSIONS

Nanocrystalline WO_3 thin films were fabricated by reactive magnetron sputter-deposition by varying the ratio of argon to oxygen in a wide range. The surface chemical composition, valence state of W ions, surface/interface chemistry, density and optical properties of nanocrystalline WO_3 films were evaluated as function of oxygen concentration in the sputtering gas mixture. The results indicate that the effect of oxygen during deposition is significant on the ultramicrostructure in terms of surface/interface chemistry. This consequently influences the optical properties of WO_3 films. Formation of stoichiometric WO_3 with tungsten existing in W^{6+} state for all WO_3 films is evident. However, WO_3 films grown at high oxygen concentration (>60%) were over stoichiometric with excess oxygen incorporated. XRR data coupled with simulations indicate that the density of WO_3 films is sensitive to the oxygen concentration. The density varies from 4.98 to 5.98 g/cm^3 with increasing Γ values form 0.5 to 1.0. The spectral transmission and band gap of the WO_3 films increases with the increasing oxygen content in the reactive gas mixture. The band gap increases from 2.75 to 3.25 eV with increasing oxygen concentration. The corresponding density of WO_3 films also exhibit the similar variation as a function oxygen content indicating a direct relationship between the oxygen concentration, density and band gap. A direct correlation between the film-density and band gap in nanocrystalline WO_3 films is presented and explained on the basis of excess oxygen incorporation and negative ion effects as encountered in the sputter-deposition process at higher oxygen pressures.

■ AUTHOR INFORMATION

Corresponding Author

*E-mail: rvchintalapalle@utep.edu.

■ ACKNOWLEDGMENTS

This material is based on the work supported by the Department of Energy under Award DE-PS26-08NT00198-00. A portion of the research presented in this manuscript was performed using Environmental Molecular Sciences Laboratory (EMSL), a national scientific user facility sponsored by the Department of Energy's Office of Biological and Environmental Research and located at Pacific Northwest National Laboratory.

■ REFERENCES

(1) Granqvist, C. G. *Handbook of Inorganic Electrochromic Materials*; Elsevier: New York, 1995.

(2) Zhang, Y.; Lee, S. H.; Mascarenhas, A.; Deb, S. K. *Appl. Phys. Lett.* **2008**, *93*, 203508.

(3) Ramana, C. V.; Utsunomiya, S.; Ewing, R. C.; Julien, C. M.; Becker, U. *J. Phys. Chem. B* **2006**, *110*, 10430.

(4) Berggren, L.; Jonsson, J. C.; Niklasson, G. A. *J. Appl. Phys.* **2007**, *102*, 083523.

(5) Lin, Y. S.; Chen, H. T.; Lai, J. Y. *Thin Solid Films* **2009**, *518*, 1377.

(6) Lu, D.; Chen, J.; Chen, H. J.; Gong, J.; Deng, S. Z.; Xu, N. S.; Liu, Y. L. *Appl. Phys. Lett.* **2007**, *90*, 041919.

(7) Lee, D. S.; Han, S. D.; Lee, D. D. *Sens. Actuators, B* **1999**, *60*, 57.

(8) Baeck, S. H.; Jaramillo, T.; Stucky, G. D.; McFarland, E. W. *Nano Lett.* **2002**, *2*, 831.

(9) Lee, D. S.; Nam, K. H.; Lee, D. D. *Thin Solid Films* **2000**, *375*, 142.
(10) Wang, L.; Teleki, S. E.; Pratsinis, S. E.; Gouma, P. I. *Chem. Mater.* **2008**, *20*, 4794.
(11) Kawasaki, H.; Namba, J.; Iwatsuji, K.; Suda, Y.; Wada, K.; Ebihara, K.; Ohshima, T. *Appl. Surf. Sci.* **2002**, *8065*, 1.
(12) Ionescu, R.; Llobet, E.; Brezmes, J.; Vilanova, X.; Correig, X. *Sens. Actuators, B* **2003**, *95*, 182.
(13) Moulzolf, S. C.; Ding, S.; Lad, R. J. *Sens. Actuators, B* **2000**, *67*, 1.
(14) Satnkova, M.; Vilanova, X.; Llobet, E.; Calderer, J.; Bittencourt, C.; Pireaux, J. J.; Correig, X. *Sens. Actuators, B* **2005**, *105*, 271.
(15) Xie, G.; Yu, J.; Chen, X.; Jiang, Y. *Sens. Actuaors, B* **2007**, *123*, 909.
(16) Santucci, S.; Cantalini, C.; Crivellari, M.; Lozzi, L.; Ottaviano, L.; Passacantanso, M. *J. Vac. Sci. Technol. A* **2000**, *18*, 1077.
(17) Gouma, P. I.; Kalyanasundaram, K. *Appl. Phys. Lett.* **2008**, *93*, 244102.
(18) Huelser, T. P.; Lorke, A.; Ifeacho, P.; Wiggers, H.; Schulz, C. *J. Appl. Phys.* **2007**, *102*, 124305.
(19) Marsen, B.; Miller, E. L.; Paluselli, D.; Rocheleau, R. E. *Int. J. Hydrogen Energy* **2007**, *32*, 3110.
(20) Paluselli, D.; Marsen, B.; Miller, E. L.; Rocheleau, R. E. *Electrochem. Solid-State Lett.* **2005**, *8*, G 301.
(21) Sun, Y.; Murphy, C. J.; Reyes-Gil, K. R.; Reyes-Garcia, E. A.; Thornton, J. M.; Morris, N. A.; Raftery, D. *Int. J. Hydrogen Energy* **2009**, *34*, 8476.
(22) Zheng, H.; Tachibana, Y.; Kalantar-Zadeh, K. *Langmuir* **2010**, *26*, 19148.
(23) Zheng, H.; Ou, J. Z.; Strano, M. S.; Kaner, R. B.; Mitchell, A.; Kalantar-Zadeh, K. *Adv. Fun. Mater* **2011**, *21*, 2175.
(24) Sahle, W.; Nygren, M. *J. Solid State Chem.* **1983**, *48*, 154.
(25) Berak, J. M.; Sienko, M. J. *J. Solid State Chem.* **1970**, *2*, 109.
(26) Salje, E.; Viswanathan, K. *Acta Crystallogr., Sect. A* **1975**, *31*, 356−359.
(27) Vogt, T.; Woodward, P. M.; Hunter, P. A. *J. Solid State Chem.* **1999**, *144*, 209.
(28) Cazzanelli, E.; Vinegoni, C.; Mariotto, G.; Kuzmin, G.; Purans, J. *J. Solid State Chem.* **1999**, *143*, 24.
(29) Chatten, R.; Chadwick, A.; Rougier, A.; Lindan, J. *J. Phys. Chem. B* **2005**, *109*, 3146.
(30) Lassner, E.; Schubert, W. D. *Tungsten: Properties, Chemistry, Technology of the Element, Alloys, and Chemical Compounds*; Kluwer Academic: New York, 1999.
(31) Cora, F.; Stachiotti, M. G.; Catlow, C. R. A.; Rodriguez, C. O. *J. Phys. Chem.* **1997**, *101*, 3945.
(32) Rao, C. N. R.; Raveau, B. *Transition Metal Oxides*; VCH: Weinheim, Germany, 1995.
(33) Chawla, A. K.; Singhal, S.; Gupta, H. O.; Chandra, R. *Thin Solid Films* **2009**, *518*, 1430.
(34) Gullapalli, S. K.; Vemuri, R. S.; Ramana, C. V. *Appl. Phys. Lett.* **2010**, *96*, 171903.
(35) Kalidindi, N. R.; Manciu, F. S.; Ramana, C. V. *ACS Appl. Mater. Interfaces* **2011**, *3*, 863.
(36) Vemuri, R. S.; Kamala Bharathi, K.; Gullapalli, S. K.; Ramana, C. V. *ACS Appl. Mater. Interfaces* **2010**, *2*, 2623.
(37) Vasilopoulou, M.; Palilis, L. C.; Georgiadou, D. G.; Argitis, P.; Kennou, S.; Kostis, I.; Papadimitropoulos, G.; Stathopoulos, N. A.; Iliadis, A. A.; Konofaos, N.; Davazoglou, D. *Thin Solid Films* **2011**, *519*, 5748.
(38) Papadimitropoulos, G.; Vourdas, N; Giannakopoulos, K.; Vasilopoulou, M.; Davazoglou, D. *J. Appl. Phys.* **2011**, *109*, 103527.
(39) Beydaghyan, G.; Bader, G.; Ashrit, P. V. *Thin Solid Films* **2008**, *516*, 1646.
(40) Gillet, M.; Aguir, K.; Lemire, C.; Gillet, E.; Schierbaum, K. *Thin Solid Films* **2004**, *467*, 239.
(41) Jerman, M.; Mergel, D. *Thin Solid Films* **2007**, *515*, 6904.
(42) Jerman, M.; Qiao, Z.; Mergel, D. *Appl. Opt.* **2005**, *44*, 3006.
(43) Mergel, D. *Thin Solid Films* **2001**, *397*, 216.
(44) Charton, P.; Gengembre, L.; Armand, P. *J. Solid State Chem.* **2002**, *168*, 175.
(45) Dupin, J. C.; Gonbeau, D.; Vinatier, P.; Levasseur, A. *Phys. Chem. Chem. Phys.* **2000**, *2*, 1319.
(46) Shpak, A. P.; Korduban, A. M.; Medvedskij, M. M.; Kandyba, V. O. *J. Electron Spectrosc. Relat. Phenom.* **2007**, *156−158*, 172.
(47) Katrib, A.; Hemming, F.; Wehrer, P.; Hilaire, L.; Maire, G. *J. Electron Spectrosc. Relat. Phenom.* **1995**, *76*, 195.
(48) Leftheriotis, G.; Papaefthimiou, S.; Yianoulis, P.; Siokou, A.; Kefalas, D. *Appl. Surf. Sci.* **2003**, *218*, 276.
(49) Kamala Bharathi, K.; Noor-A-Alam, M.; Vemuri, R. S.; Ramana, C. V. *RSC Adv.* **2012**, *2*, 941.
(50) Subrahmanyam, A.; Karuppasamy, A. *Sol. Energy Mater. Sol. Cells* **2007**, *91*, 266.
(51) Tahar, R. B. H.; Ban, T.; Ohya, Y.; Takahashi, Y. *J. Appl. Phys.* **1998**, *83*, 2631.
(52) Niklasson, G. A.; Granqvist, C. G. *J. Mater. Chem.* **2007**, *17*, 127.
(53) Koffyberg, F. P.; Dwight, K.; Wold, A. *Solid State Commun.* **1979**, *30*, 433.
(54) Vuoristo, P.; Matyla, T.; Kettunen, P.; Lappalainen, R. *Thin Solid Films* **1991**, *204*, 297.
(55) Chin, C. C.; Lin, R. J.; Yu, Y. C.; Wang, C. W.; Lin.; Tsai, W. C.; Tseng, T. C. *Physica C* **1996**, *260*, 86.
(56) Venk, T. J.; Boonekamp, E. P.; Verbeek, R. G. F. A.; Tamminga, Y. *J. Appl. Phys.* **1999**, *85*, 1540.
(57) Uthanna, S.; Subramanyam, T. K.; Srinivasulu Naidu, B.; Mohan Rao, G. *Opt. Mater.* **2002**, *19*, 461.
(58) Hashimoto, S.; Matsuoka, H. *J. Electrochem. Soc.* **1991**, *138*, 2403.
(59) Hashimoto, S.; Matsuoka, H. *Surf. Interface Anal.* **1992**, *19*, 464.